

# Synthesis, characterization, electronic structure, and phonon properties of the noncentrosymmetric superconductor LaPtSi

F. Kneidinger, H. Michor, A. Sidorenko, and E. Bauer

*Institute of Solid State Physics, Vienna University of Technology, A-1040, Wien, Austria*

I. Zeiringer and P. Rogl

*Institute of Physical Chemistry, University of Vienna, Währingerstrasse 42, A-1090, Wien, Austria*

C. Blaas-Schenner, D. Reith, and R. Podloucky

*Institute of Physical Chemistry, University of Vienna and Center for Computational Materials Science, Sensengasse 8, A-1090, Wien, Austria*

(Received 14 June 2013; revised manuscript received 16 August 2013; published 9 September 2013)

In the present work we report on the synthesis, crystal structure, and physical properties (resistivity, magnetization, heat capacity) in combination with density functional theory (DFT) calculations of the electronic structure and phonon properties for the intermetallic compound LaPtSi. LaPtSi crystallizes in its own noncentrosymmetric structure type (space group  $I4_1md$ ;  $a = 0.42502(1)$  nm and  $c = 1.4525(5)$  nm), which is an ordered ternary derivative of the centrosymmetric  $\alpha$ -ThSi<sub>2</sub>-structure. The weakly correlated compound LaPtSi (Sommerfeld value  $\gamma = 6.5$  mJ/molK<sup>2</sup>) exhibits superconductivity below  $T_c = 3.35$  K and appears to be a fully gapped, weakly coupled  $s$ -wave BCS superconductor. The experimental observations are supported by DFT calculations which show that, despite a substantial spin-orbit splitting of the Fermi surfaces, a spin-singlet pairing is prevalent.

DOI: [10.1103/PhysRevB.88.104508](https://doi.org/10.1103/PhysRevB.88.104508)

PACS number(s): 74.25.Bt, 74.70.Ad, 72.15.Eb

## I. INTRODUCTION

Since the discovery of superconductivity in the noncentrosymmetric heavy fermion compound CePt<sub>3</sub>Si (Ref. 1) superconductivity in noncentrosymmetric intermetallic compounds with or without strong correlations among electronic states has reached widespread research interest. Here, the absence of an inversion center along with the parity violating antisymmetric spin-orbit coupling (ASOC) enables a mixture of spin-singlet and spin-triplet components in the superconducting condensate. Unconventional behavior, like zeros in the superconducting gap function, is possible also if the pair wave function has the full spatial symmetry of the crystal.<sup>2</sup>

The present study aims at a further check of materials, whether or not strong electron correlations are the primary cause of unconventional superconductivity occurring in materials without inversion symmetry. LaPtSi is selected for this goal because the heavy element Pt promotes a significant spin-orbit coupling, lifting the two-fold spin-degeneracy of electronic bands.

The crystal structure of ternary noncentrosymmetric LaPtSi has already been described by Klepp and Parthe<sup>3</sup> from single crystal investigations. Evers *et al.*<sup>4</sup> reported superconductivity in LaPtSi with a superconducting transition temperature of 3.3 K. Ramakrishnan and coworkers<sup>5</sup> studied the superconducting properties of LaPtSi in some detail, revealing  $T_c = 3.8$  K from resistivity, specific heat, and susceptibility measurements. Additionally, magnetic pair breaking was studied by these authors by substituting La with Ce and Nd. However, no investigations have been made concerning the absence of inversion symmetry. The isotopic compound CePtSi has been classified by Lee and Shelton<sup>6</sup> as a heavy fermion and coherent dense Kondo lattice system without a magnetic or superconducting transition down to 70 mK.

The aims of the present study are to investigate the superconducting compound concerning the lack of inversion symmetry in its crystal structure and to understand the superconducting properties in combination with density functional theory (DFT) calculations.

## II. EXPERIMENTAL AND COMPUTATIONAL DETAILS

Polycrystalline samples were prepared by arc melting the stoichiometric amounts of pure metal ingots under Ti-gettered argon. To ensure homogeneity of the samples, they were turned over and remelted several times. All samples were sealed in quartz ampoules under a vacuum and annealed at 800° C for one week. For sample characterization x-ray powder diffraction (XRD), scanning electron microscopy (SEM), and electron probe microanalysis (EPMA) has been used. Details on characterization techniques are summarized in Ref. 7. Resistivity measurements were performed in a cryogenic <sup>3</sup>He setup from 350 mK to room temperature at magnetic fields up to 12 Tesla. Samples were prepared as thin bars and mounted parallel to the magnetic field. Four gold wires were connected by spot welding. The electrical resistivity was measured by an a.c. resistance bridge (Lakeshore 370). For the specific heat measurements a conventional Quantum Design PPMS with a <sup>3</sup>He inset down to 400 mK on a relaxation-time calorimeter with heat pulses of around 2% and a 9 T magnet was used. Flat, highly polished, quadratic samples of around 40 mg were fixed with Apiezon N grease on the  $\alpha$ -Al<sub>2</sub>O<sub>3</sub> measurement platform. Magnetization was measured employing a cryogenic superconducting quantum interference device (SQUID) magnetometer (S700X) at temperatures from 1.8 to 5 K. The sample used was cylindrical with an aspect ratio of 1:2 (diameter to length) and was mounted parallel to the applied field.

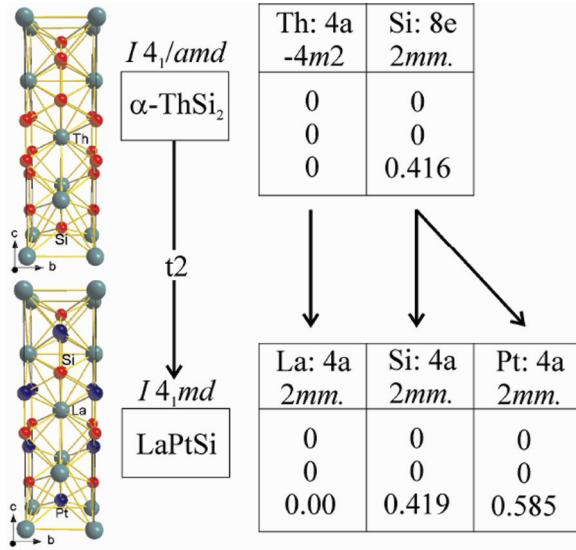


FIG. 1. (Color online) Group-subgroup relations for  $\text{ThSi}_2$ - $\text{LaPtSi}$  and the unit cells of these compounds.

The DFT calculations were done using the Vienna *ab initio* simulation package (VASP)<sup>8,9</sup> utilizing the pseudopotential construction according to the projector augmented wave method.<sup>10</sup> For the exchange-correlation functional the local density approximation (LDA) as parametrized by Ceperley and Alder<sup>11</sup> was chosen. The size of the basis set was defined by an energy cutoff of 245.7 eV. The Brillouin-zone integration for the computation of total energies was made using a Gaussian smearing with  $\sigma = 0.2$  eV on a  $11 \times 11 \times 11$  Monkhorst and Pack<sup>12</sup>  $k$ -point mesh.

The vibrational properties were calculated within the harmonic approximation by making use of the direct force-constant method as implemented in our program package full-symmetry PHON (fPHON), which is based on the package PHON.<sup>13</sup> To derive the force constants atomic displacements of 0.02 Å were chosen. Before applying such displacements the structural parameters (i.e., the volume and shape of the unit cell as well as the positions of the atoms within the unit cell) were relaxed until the residual forces were less than  $10^{-4}$  eV/Å and furthermore a suitable supercell was constructed. Because  $\text{LaPtSi}$  as a ternary derivative of the  $\alpha$ - $\text{ThSi}_2$ -type has a body-centered tetragonal primitive crystal structure containing six atoms in the asymmetric unit cell, a supercell that contains 48 atoms was constructed.

### III. RESULTS AND DISCUSSION

#### A. Structural details

Ternary  $\text{LaPtSi}$  (space group  $I4_1md$ ) belongs to an ordered ternary derivative structure type of the  $\alpha$ - $\text{ThSi}_2$ -type (space group  $I4_1/amd$ ;  $a = 0.4126$  nm,  $c = 1.4346$  nm) (Ref. 3). The corresponding group-subgroup relation in the form of a Bärnighausen tree<sup>14,15</sup> is shown in Fig. 1. Note that in this case, a nonstandardized setting is used. A Rietveld refinement of the x-ray pattern observed for  $\text{LaPtSi}$  at room temperature is shown in Fig. 2. Corresponding crystallographic data are summarized in Table I. The lattice parameters obtained in this

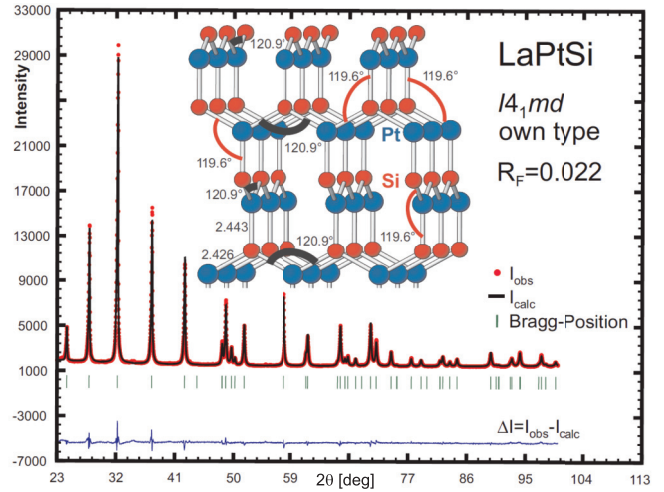


FIG. 2. (Color online) Rietveld refinement for  $\text{LaPtSi}$  (standardized setting). The inset shows structural details of  $\text{LaPtSi}$ .

work are in excellent agreement with data reported previously in Ref. 3.

The inset in Fig. 2 shows the three-dimensional Si-Pt framework formed by two sets of perpendicular Si-Pt zig-zag chains. Intrachain and interchain distances are rather homogeneous. Also, the Pt-Si-Pt bond angles are almost identical, with only a slight deviation from  $120^\circ$ . This reflects the fact that  $\text{LaPtSi}$  is an ordered representative of the  $\alpha$ - $\text{ThSi}_2$ -type structure, which in turn is a shift variant of the hexagonal  $\text{AlB}_2$  type.

A comparison of our calculated (DFT) structural parameters to our experimental values in Table I shows both in excellent agreement, the Wyckoff positions and the  $c/a$  ratio of 3.42 are almost identical. Regarding the lattice parameters a slight underestimation of about 1% by the DFT-LDA as compared to experiment is noticeable.

#### B. Physical properties

As reported in Refs. 4–6,16  $\text{LaPtSi}$  exhibits superconductivity. The values of the superconducting transition temperatures reported in the literature scatter between 3.18 and 3.8 K (Refs. 4–6,16) agreeing well with  $T_c = 3.35$  K from the present specific heat measurement.

Electrical resistivity ( $\rho$ ) measurements on polycrystalline  $\text{LaPtSi}$  were carried out from 350 mK to room temperature, with  $\rho_{300\text{K}} = 230 \mu\Omega\text{cm}$  (data below 80 K are displayed

TABLE I. Structural parameters and Wyckoff positions of  $\text{LaPtSi}$ .

	Exp.	DFT
Lattice parameter $a$ :	0.42502(1) nm	0.420 nm
Lattice parameter $c$ :	1.4525(5) nm	1.436 nm
La on 4a	$z$ : 0.5805(4)	0.5804
Pt <sup>a</sup> on 4a	$z$ : 0.1670(3)	0.1680
Si <sup>b</sup> on 4a	$z$ : 0.0	0.0
Crystal structure:	ternary derivative of $\alpha$ - $\text{ThSi}_2$	
Space group:	109 or $I4_1md$	

<sup>a</sup>Pt\* = 3.94Pt + 0.06(3)Si.

<sup>b</sup>Si\* = 3.93Si + 0.07(4)Pt.

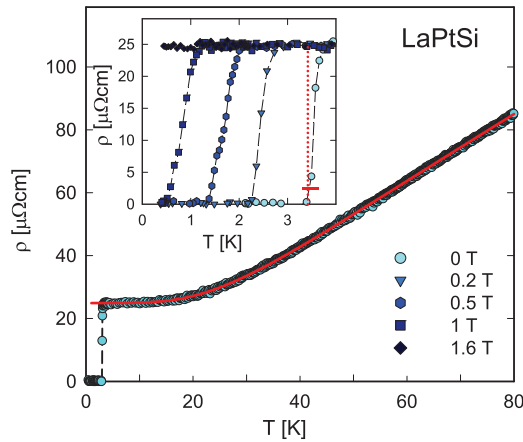


FIG. 3. (Color online) Temperature-dependent electrical resistivity  $\rho$  of LaPtSi. The solid line is a least-squares fit as explained in the text. The inset shows the magnetic field dependence of the resistive superconducting transition. The dotted line indicates the phase transition temperature at  $\mu_0 H = 0$  T.

in Fig. 3). The respective residual-resistivity-ratio  $R \approx 9$ , together with the relatively small width of the superconducting phase transition temperature refer to fairly good sample quality.

Below 3.65 K the electrical resistivity of LaPtSi drops from around  $25 \mu\Omega\text{cm}$  to zero (see inset, Fig. 3), indicating a second-order phase transition into the superconducting state. The transition temperature was identified at 10% of the residual resistivity at 3.42 K. The resistivity curve above  $T_c$  follows a metallic behavior and was accounted for in terms of the Bloch-Wilson model,<sup>17</sup> which, in addition to the standard Bloch-Grüneisen law, incorporates phonon assisted  $s$ - $d$  scattering. This last mechanism originates a  $T^3$  temperature component for low temperatures, being appropriate to account for the experimental data of LaPtSi with  $d$  states resulting from Pt and La. A least-squares fit of this model, i.e.,

$$\rho(T) = A \left( \frac{T}{\theta_D} \right)^5 \int_0^{\theta_D/T} \frac{z^5 dz}{[\exp(z) - 1][1 - \exp(-z)]} + B \left( \frac{T}{\theta_D} \right)^3 \int_{\theta_{\min}/T}^{\theta_D/T} \frac{z^3 dz}{[\exp(z) - 1][1 - \exp(-z)]}, \quad (1)$$

to the experimental data (solid line, Fig. 3) reveals a Debye temperature  $\theta_D = 152$  K, as well as a minimum phonon energy  $k_B \theta_{\min} = \hbar \omega_{\min}$ , with  $\theta_{\min} = 77$  K. Here,  $\omega_{\min}$  is the frequency corresponding to the minimum  $\vec{q}$  value to excite the  $s$ - $d$  transitions.<sup>17</sup>  $A = 230 \mu\Omega\text{cm}$  and  $B = 160 \mu\Omega\text{cm}$  are material-dependent constants. A description in terms of the parallel resistance model to  $\rho(T)$  of LaPtSi, as was also executed by Ramakrishnan *et al.*,<sup>5</sup> generates for the present resistivity data set a Debye temperature of 169 K. Both values assessed are well below the Debye temperature derived from the specific heat measurement ( $\theta_D^{L_T} = 245$  K, see below).

The discrepancies in the absolute numbers of the Debye temperatures between resistivity and specific heat analyses are frequently observed for intermetallic compounds. The primary cause for this fact might be the difference in the temperature ranges considered: while heat capacity data are usually analyzed only in a narrow temperature range (below

about 10 K and thus sensing low- $\vec{q}$  acoustic phonon excitations only),  $\rho(T)$  analyses extend over the entire measured range up to 300 K where thermal excitations involve the whole phonon spectrum. Consequently, the discrepancy between the values of the Debye temperature extracted from specific heat and resistivity refer to a significant difference between the actual phonon DOS and that of the simple Debye model [see our *ab initio* calculation of the phonon density of states (DOS) in Sec. III D]. The differences are in general substantial if strongly curved  $\rho(T)$  data sets are taken into consideration, where, e.g., Mott-Jones type scattering<sup>18</sup> processes cause at high temperatures strong deviations from the  $T$ -linear dependence of simple metallic systems.

A comparison of the present  $\rho(T)$  data to those of Ramakrishnan *et al.*<sup>5</sup> evidences a much smaller room temperature value but a slightly larger residual resistivity of the present sample resulting in a larger  $R$  value for the material used in Ref. 5. These differences might be an implication of some preferred orientation of grains in the polycrystalline sample. Given that LaPtSi is rather anisotropic ( $c/a = 3.42$ ) a preferred orientation can favor either basal plane or  $c$ -axis components arranged in the electrical current direction at the  $\rho(T)$  measurement. Consequently, a substantial variation of  $\rho(T)$  data of samples with comparable quality is possible.

As indicated in Table I, there is x-ray evidence for a nonnegligible site-interchange of Si and Pt on the  $4a$  sites in the crystalline unit cell. The resulting partial disorder can then be made responsible for the somewhat larger residual resistivity of the sample studied, rather than impurity phases. This fact is backed from the absence of any traces of impurities in the x-ray pattern (Fig. 2) and the excellent agreement with model calculations (solid line, Fig. 2) employing the LaPtSi phase only.

The inset of Fig. 3 demonstrates the suppression of superconductivity in LaPtSi upon the application of external magnetic fields. The  $\mu_0 H = 1.6$  T run does not reveal any indication of superconductivity above 350 mK. As displayed in the inset, the width of the transition increases with the applied field. Such a behavior has been found in various noncentrosymmetric superconductors like  $\text{Li}_2\text{Pd}_3\text{B}$  (Ref. 19),  $\text{Mg}_{10}\text{Ir}_{19}\text{B}_{16}$  (Ref. 20),  $\text{BaPtSi}_3$  (Ref. 21), or  $\text{YNiGe}_3$  (Ref. 22), just to mention a few.

Bulk superconductivity at 3.35 K is proven by measurements of the specific heat (Fig. 4). Entropy balance was used as a constraint to determine the superconducting transition temperature, i.e., comparing the values where the entropy in the SC state and the entropy in the field suppressed state are equal. The transition appears to be slightly broadened due to the applied heat pulses of around 2% of the absolute temperature. The application of an external magnetic field leads to a suppression of the superconducting transition at  $H_{c2}^{C_p} \approx 0.45$  T in heat capacity measurements. From a low temperature fit of the specific heat according to  $C_p = \gamma T + \beta T^3$  at  $\mu_0 H = 1.6$  T, the Sommerfeld value  $\gamma = 6.5$  mJ/molK<sup>2</sup> and  $\beta = 0.39$  mJ/molK<sup>4</sup> were determined, yielding a Debye temperature  $\theta_D^{L_T}$  of 245 K, which is in close agreement with the values calculated in Ref. 5.

The jump of the specific heat  $(C_{es} - C_{en})/(\gamma T_c)$  at the superconducting transition reveals a value of 1.37 which is in rather good agreement with the BCS ratio of 1.43, reflecting

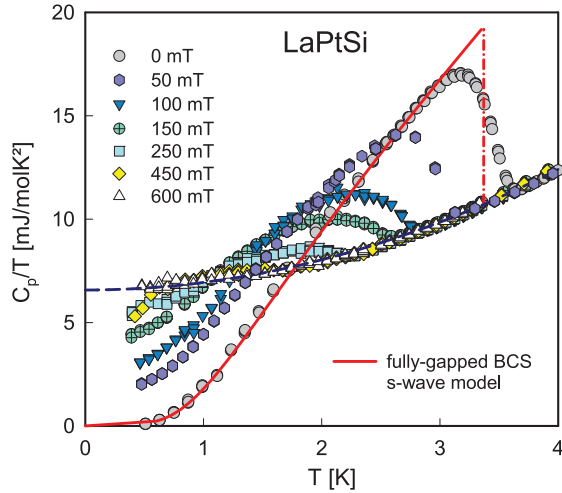


FIG. 4. (Color online) Temperature-dependent specific heat of LaPtSi for various values of applied magnetic fields. The dashed-dotted line refers to the ideal superconducting transition at  $T = 3.35$  K, while the solid line is the temperature-dependent heat capacity of a fully gapped  $s$ -wave BCS superconductor. The dashed line refers to a low temperature extrapolation of the heat capacity data in the normal state.

weak coupling. As demonstrated in Fig. 4 the numerical values of the BCS theory as calculated by Mühlischlegel<sup>23</sup> are close to the experimental results and, therefore, indicate conventional Cooper pairing with an exponential decay of  $C_p(T)$  at low temperatures. This, in general, characterizes a fully gapped  $s$ -wave superconductor.

Low temperature magnetization measurements on LaPtSi have been carried out in a field cooling (FC) and zero field cooling (ZFC) mode at various externally applied magnetic fields (see Fig. 5). The rapid drop of the ZFC data below 3.15 K denotes the onset of superconductivity, in fair agreement with resistivity and heat capacity data. Given that the demagnetization factor of the sample lies between 0.2 and 0.1, the ZFC results indicate that the shielding of the superconducting

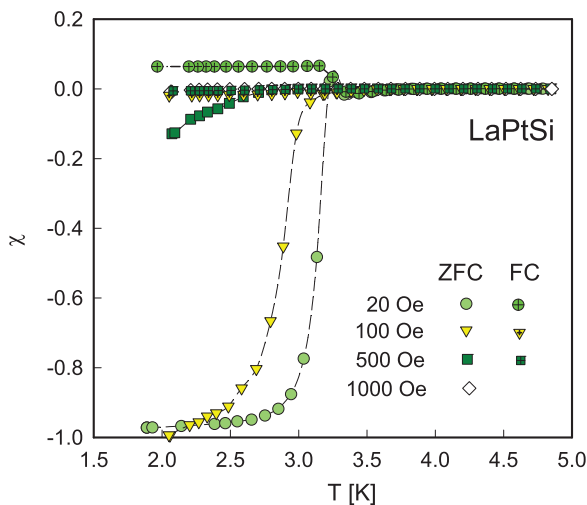


FIG. 5. (Color online) Low temperature (1.8 to 5 K) magnetic susceptibility ( $\chi$ ) of LaPtSi taken at various fields for zero field cooling and field cooling.

volume in LaPtSi covers a fraction between 89% and 100% ( $\chi = -1$ ) of the sample, respectively.

In the case of FC measurements, flux pinning centers tend to trap magnetic flux. As a result, the susceptibility in the superconducting state remains small. Thus, the distinct differences in both the ZFC and the FC case validate type-II bulk superconductivity below 3.15 K in LaPtSi.

The upper critical magnetic field  $\mu_0 H_{c2}$  of LaPtSi as derived from both resistivity and heat capacity data is plotted in Fig. 6. While at low fields both quantities agree well, the superconducting transition temperatures are quite different in the high field limit. Predominantly three mechanisms are known to account for this observation, (i) the anisotropy of the upper critical magnetic field; (ii) surface effects, which give rise to  $\mu_0 H_{c3}$ , or (iii) filamentary effects as was discussed in detail, e.g., for noncentrosymmetric  $\text{Mg}_{10}\text{Ir}_{19}\text{B}_{16}$  by Klimczuk *et al.*<sup>20</sup> Here, the much stronger scattering of electrons at grain boundaries causes a reduced electronic mean free path, which in turn governs the superconducting coherence length, thus rising  $\mu_0 H_{c2}$  above the intrinsic values. Taking into account the bulk data as derived from heat capacity measurements,  $\mu_0 H_{c2}$  extrapolates to  $\approx 0.4$  T for  $T = 0$  with an initial slope  $\mu_0 H_{c2}' = -0.17$  T/K. The Werthamer-Helfand-Hohenberg (WHH) theory<sup>24</sup> describes the upper critical magnetic field by taking into account orbital pair breaking as well as Pauli limiting, employing two parameters, the Maki parameter  $\alpha$  and the spin-orbit coupling strength  $\lambda_{\text{so}}$ . While  $\alpha = 0.11$  can be calculated from the knowledge of the residual resistivity  $\rho_0$  and the Sommerfeld constant  $\gamma$ ,  $\lambda_{\text{so}}$  is a fit parameter. Note that while a finite value of  $\alpha$  reduces  $\mu_0 H_{c2}(0)$ , an increasing value of  $\lambda_{\text{so}}$  recovers the  $\alpha = 0$  scenario. Setting  $\lambda_{\text{so}} = 10$ , reveals a convincing fit to the experimental data (solid line, Fig. 6). Since, however,  $\lambda_{\text{so}}$  does not significantly change  $\mu_0 H_{c2}(T)$  if  $\alpha$  is small, a modeling of the experimental  $\mu_0 H_{c2}(T)$  data with  $\lambda_{\text{so}} = 0$  does not reveal noticeable changes (small diamonds, Fig. 6).

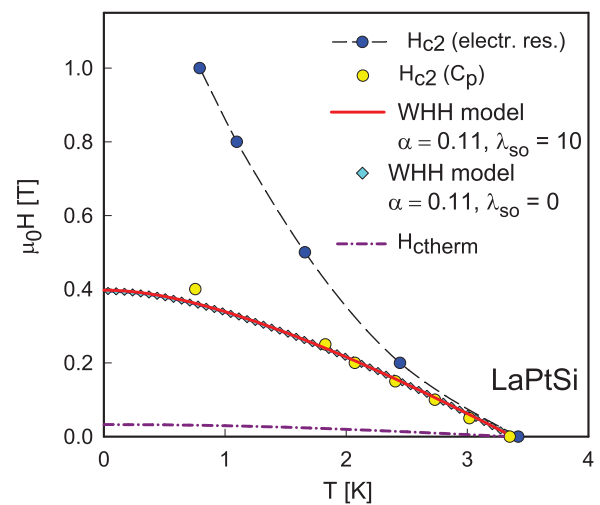


FIG. 6. (Color online) Upper critical magnetic field of LaPtSi as derived from resistivity and heat capacity data. The solid line and the small diamonds are fits according to the WHH model and the dashed-dotted line displays the temperature dependent thermodynamic critical field  $\mu_0 H_c$ . The dashed line is a guide for the eyes.

The rather small value of the Maki parameter hints to the absence of Pauli limiting. A simplified expression of the Pauli limiting field, i.e.,  $H_p = 1.86T/K \cdot T_c$  yields 6.2 T, far above the experimental value. Thus the upper critical magnetic field of LaPtSi is limited almost entirely by orbital pair breaking.

As already mentioned above, the significant  $c/a$  crystal anisotropy may cause a substantial anisotropy of the upper critical field. Moreover, the preferred orientation of grains can influence a simple polycrystalline average of the upper critical field  $[\mu_0 H_{c2}^{\text{poly}} = (2/3)\mu_0 H_{c2}^{a,b} + (1/3)\mu_0 H_{c2}^c]$  such that in resistivity measurements a certain crystallographic direction is favored on the cost of the other. Additionally, anisotropy can contribute to a moderate broadening of the superconducting transition upon increasing external magnetic field as indeed is observed for both the resistive as well as heat capacity anomalies. From the latter we evaluate an upper limit for the anisotropy of the upper critical field slopes of about 30%.

The integration of the entropy difference from the superconducting and the normal state gives the difference in the free energy,  $\Delta F = F_n - F_s$ , being proportional to the thermodynamical critical field, i.e.,

$$\Delta F(T) = \frac{\mu_0 H_c^2(T)}{2} = \int_{T_c}^T \int_{T_c}^{T'} \frac{C_s - C_n}{T''} dT'' dT' \quad (2)$$

revealing  $\mu_0 H_c = 33$  mT when extrapolating towards  $T = 0$  (the dashed-dotted line, Fig. 6).

The knowledge of the thermodynamical critical field allows to evaluate a value for the dimensionless Ginzburg-Landau parameter  $\kappa_{GL} = H_{c2}(0)/(\sqrt{2}H_c) \simeq 8.7$ , where the WHH value for  $H_{c2}(0) = 0.41$  T has been used. The coherence length  $\xi_0$  for  $T \rightarrow 0$  can be obtained from  $\mu_0 H_{c2} = \Phi_0/(2\pi\xi_0^2)$ , yielding  $\xi_0 \simeq 2.83 \times 10^{-8}$  m. Combining the Ginzburg-Landau parameter with the coherence length, the London penetration depth can be obtained as  $\lambda_L(T \rightarrow 0) \simeq 2.5 \times 10^{-7}$  m. It should be noted that these values deviate slightly from the parameters as reported in Ref. 5. This reflects the discrepancy in the values of  $H_{c2}^{CP}$  and  $H_{c2}^{es}$  since the data in Ref. 5 are taken from resistivity measurements only.

Based on  $l_{tr}/\xi \approx 0.92$  LaPtSi can be classified as a superconductor in the dirty limit ( $l_{tr}$  is the total elastic mean free path).

### C. Electronic structure

In Fig. 7 the electronic band structure and density of states (DOS) and in Fig. 8 the Fermi surfaces are shown calculated both in a scalar relativistic approximation, omitting spin-orbit coupling, and fully relativistically, including spin-orbit coupling, as implemented in VASP, in a self-consistent and parameter-free manner.<sup>25</sup> The preciseness of spin-orbit coupling in the projector augmented wave method has been verified by comparing the VASP results to calculations using the all electron full-potential linearized augmented plane-wave method<sup>26,27</sup> in Ref. 28 and also cross-checked for LaPtSi.

The band structure in Fig. 7 (left panel) shows that some of the degeneracies at the high-symmetry points are lifted by taking the spin-orbit coupling into account. For example, at  $\Gamma$  a spin-orbit splitting of  $\sim 275$  meV below the Fermi energy and of  $\sim 455$  meV above the Fermi energy is obvious.

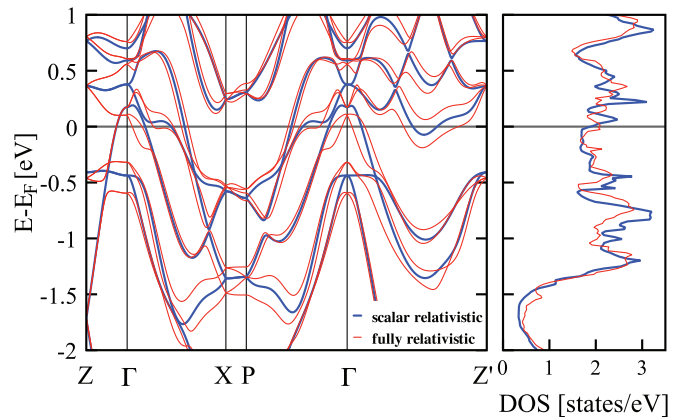


FIG. 7. (Color online) Electronic band structure and DOS per formula unit of LaPtSi calculated scalar relativistically (dark gray/blue lines) and fully relativistically including spin-orbit coupling (light gray/red lines). The energy scale is defined relative to the Fermi energy.

The lack of inversion symmetry in the crystal structure of LaPtSi gives rise to an antisymmetric spin-orbit coupling (ASOC),<sup>2,21,29,30</sup> i.e., the double (spin) degeneracy of the

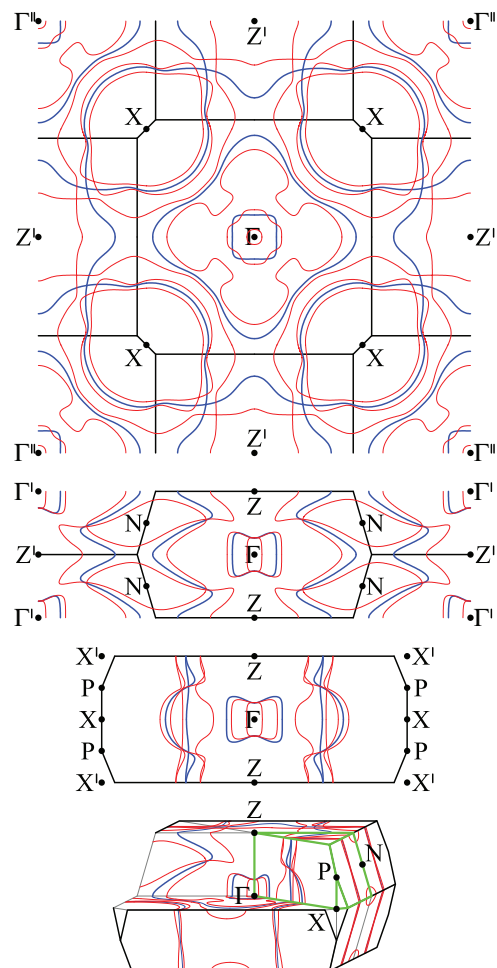


FIG. 8. (Color online) Fermi surfaces of LaPtSi calculated scalar relativistically (dark gray/blue lines) and fully relativistically including spin-orbit coupling (light gray/red lines) and the Brillouin zone of the body-centered tetragonal lattice for  $c > a$ .

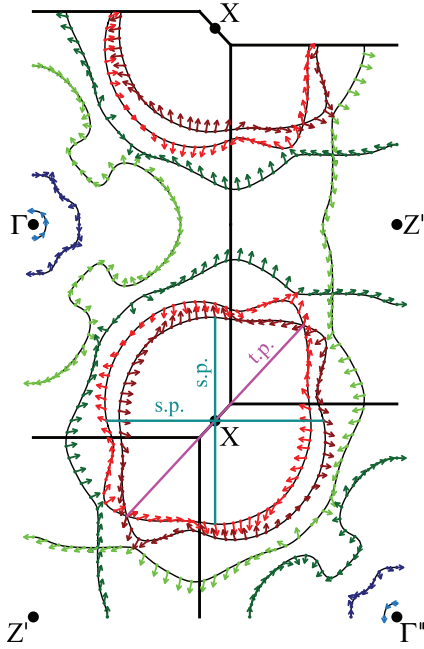


FIG. 9. (Color online) Spin directions on the Fermi surfaces of LaPtSi calculated in a fully relativistic scheme. The arrows indicate the direction and the magnitude of the spins. Note that in the plane shown the spins have no out-of-plane components. Examples for spin-singlet pairing (s.p.) and simultaneous spin-singlet and spin-triplet pairing (t.p.) are also indicated.

bands is lost due to spin-orbit coupling in noncentrosymmetric compounds. In LaPtSi the inversion center is destroyed solely by the arrangement of the atoms along the  $c$  axis. Therefore, the two-fold degeneracy of the bands along  $\Gamma$ - $Z$  is still pertained since the ASOC occurs only perpendicular to the directions that break inversion symmetry as revealed by the electronic band structure in Fig. 7. With the exception of the  $\Gamma$ - $Z$  direction an ASOC of varying size is found, for example, for the spin-orbit split band originating at  $\Gamma$  at  $\sim 170$  meV (second eigenvalue including spin-orbit coupling above the Fermi energy at  $\Gamma$ ) the vertical ASOC splitting of the bands is  $\sim 130$  meV along both  $\Gamma$ - $X$  and  $\Gamma$ - $P$  and  $\sim 255$  meV along  $\Gamma$ - $Z'$ .

Concerning the superconductivity of a noncentrosymmetric compound the horizontal ASOC splitting of the bands at the Fermi energy is of prime importance. Such a horizontal ASOC splitting can be easily seen by looking at the Fermi surfaces (Fig. 8).

Omitting spin-orbit coupling the Fermi surfaces of LaPtSi consist of three sheets: a closed hole Fermi surface around  $\Gamma$ , an irregular open hole tube around  $\Gamma$ - $Z$ , and a twisted electron pillar along  $X$ - $X'$ . Taking spin-orbit coupling into account, the ASOC gives rise to a substantial splitting of these Fermi surfaces. Along  $\Gamma$ - $Z'$  no doubling of the tube Fermi surface sheet is observed, as one of the split bands moves completely above the Fermi surface (see Fig. 7). As discussed there is no ASOC splitting along  $\Gamma$ - $Z$ , therefore the ASOC split Fermi surfaces touch along  $\Gamma$ - $Z$ .

Regarding Fig. 9 it becomes obvious that electrons on the ASOC split Fermi surfaces do not have strictly opposite spin directions. This is due to a rather strong interband spin-orbit

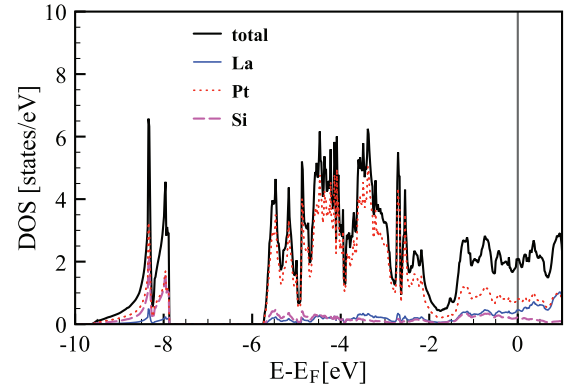


FIG. 10. (Color online) Total and atomic-projected electronic DOS per formula unit of LaPtSi calculated fully relativistically including spin-orbit coupling. The energy scale is defined relative to the Fermi energy.

coupling in LaPtSi. However, as expected the spin directions rotate along each Fermi surface sheet.

Figure 10 shows the electronic density of states (DOS) obtained from a fully relativistic calculation including spin-orbit coupling. In the range  $-6$  to  $-2$  eV below the Fermi energy the Pt- $d$  band can be identified with some hybridization of La- $d$  and Si- $p$ . At the Fermi energy the contribution of Pt is dominant, but the contributions of both La and Si cannot be neglected. The most dominant contributions are Pt- $d$ , La- $d$ , Pt- $p$ , and Si- $p$ . The DOS at the Fermi energy is mainly of  $d$  character whereby the Pt- $d$  contribution is by a factor of 1.7 larger than the La- $d$  contribution. The Pt- $p$  is about 90% of the La- $d$ , and the Si- $p$  is about 75% of the Pt- $p$ . The electronic DOS per formula unit of LaPtSi at the Fermi energy is 2.076 states/eV when spin-orbit coupling is included compared to 1.898 states/eV omitting spin-orbit coupling (see also Fig. 7), corresponding to a calculated electronic Sommerfeld value  $\gamma_e = \text{DOS}(E_F) \cdot k_B^2 \pi^2 / 3$  of 4.89 mJ/molK<sup>2</sup> for the former and 4.47 mJ/molK<sup>2</sup> for the latter.

A comparison of the experimental Sommerfeld value  $\gamma$  with the electronic one  $\gamma_e$  determined from the electronic structure calculation reveals an electron-phonon enhancement factor  $\lambda_{ep}$  via

$$\gamma = \gamma_e (1 + \lambda_{ep}) \quad (3)$$

as  $\lambda_{ep} = 0.33$  and  $0.45$ , respectively. Both parameters point to a weakly coupled superconducting state in LaPtSi.

Employing the empirical McMillan's formula<sup>31</sup>

$$T_c = \frac{\theta_D}{1.45} \exp\left(-\frac{1.04(1 + \lambda_{ep})}{\lambda_{ep} - \mu_c^*(1 + 0.62\lambda_{ep})}\right) \quad (4)$$

with our experimental value of  $T_c = 3.35$  K,  $\theta_D$  in the range 152–245 K, and the Coulomb repulsion strength  $\mu_c^*$  generally lying within 0.09–0.18, the resulting values for  $\lambda_{ep} = 0.5$ – $0.8$  also suggest weak coupling. The rather high DOS at the Fermi energy accounts for the lower values of  $\lambda_{ep}$  as extracted from Sommerfeld values compared to the values extracted from McMillan's formula.

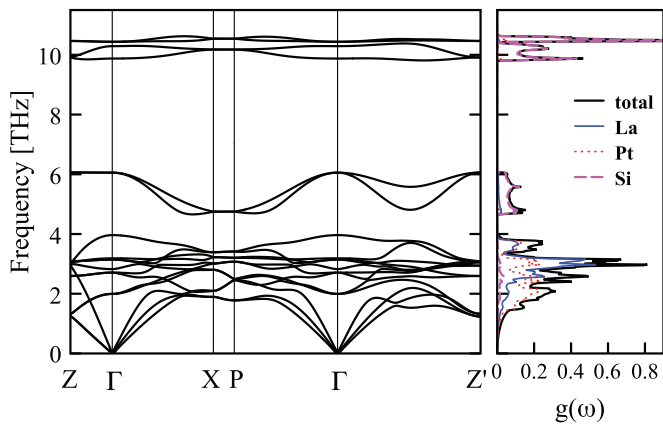


FIG. 11. (Color online) Phonon dispersion and DOS [ $g(\omega)$ ] for LaPtSi. The phonon DOS is split into the contributions of the modes attributed to La, Pt, and Si.

#### D. Vibrational properties

Considering the phonon dispersion in Fig. 11 we find that LaPtSi (see Table I for its crystal structure) is dynamically stable. About halfway along  $\Gamma$ - $Z'$  (at  $\vec{q}_{\text{soft}} \simeq 0.5 \vec{\Gamma}Z'$ ) a distinct phonon softening can be identified. This phonon softening at  $\vec{q}_{\text{soft}}$  comes along with a Fermi surface nesting as seen from Figs. 8 and 9. Frequently, such a coexistence of phonon softening and Fermi surface nesting in the normal state favors superconductivity.

Studying the normalized phonon DOS in Fig. 11 one can observe that, as expected, Si as the lightest element in the compound dominates at the higher frequencies. Specifically the ranges of 4.7–6.1 and 9.7–10.7 THz with a very pronounced peak around 10.5 THz are attributed almost entirely to Si. While Pt, as the heaviest element, dominates the lower frequencies in the range of 0–2.5 THz. The contribution of La to the phonon modes is strongest between 2.5–4.0 THz. In the whole range of 0–4 THz a strong La–Pt hybridization can be seen. Further, a much smaller Si contribution has been observed in this lower frequency range of 0–4 THz and some La and Pt contributions can be seen in the higher frequency ranges of 4.7–6.1 and 9.7–10.7 THz.

From the DFT derived phonon DOS,  $g(\omega)$ , the heat capacity is calculated using

$$C_p(T) = R \int g(\omega) \frac{\left(\frac{1}{2} \frac{h\omega}{k_B T}\right)^2}{\sinh^2\left(\frac{1}{2} \frac{h\omega}{k_B T}\right)} d\omega, \quad (5)$$

where  $\omega$  is the phonon frequency,  $k_B$  the Boltzmann constant,  $h$  the Planck constant, and  $R$  the gas constant. Regarding the accuracy of the DFT derived phonon DOS  $g(\omega)$  the specific heat capacity  $C_p(T)$  [Eq. (5)] is compared to the experimental results in Fig. 12(a). Perfect agreement is revealed, with an exception for temperatures in the range from 50 to 100 K where the experimental data are slightly below the DFT ones.

An estimation of relevant phonon branches can be derived from the specific heat data analyzed in terms of a model suggested by Junod *et al.*<sup>32,33</sup> In this model, the temperature-dependent quantity  $(C_p - \gamma T)/T^3$  allows for a straightforward inspection of deviations from the simple

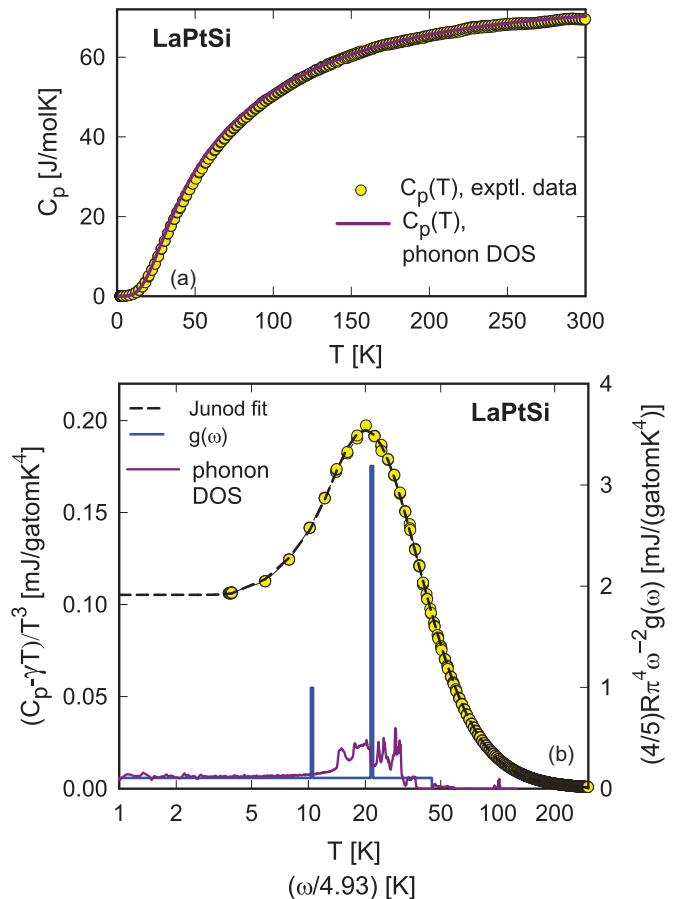


FIG. 12. (Color online) (a) Experimental and theoretical heat capacity  $C_p$  of LaPtSi. (b) A plot of  $(C_p - \gamma T)/T^3$  vs.  $\ln T$  of LaPtSi. The dashed line is a least-squares fit of the experimental data using the model described in the text. The essential parameters of the model used to construct the spectral function  $g(\omega)$  (solid lines, right axis) are  $\theta_D = 216$  K,  $\omega_{E1} = 51.4$  K with a width of 1.5 K, and  $\omega_{E2} = 106.6$  K with a width of 3.5 K.

Debye model. The approximated phonon spectrum consists of a Debye spectrum overlaid by Einstein branches with finite spectral widths. The experimental data for LaPtSi are shown in Fig. 12(b), referring to the left axis of this graph. Besides a Debye-like background, at least two Einstein branches are needed to account for the experimental findings. A least-squares fit according to Junod's model returns a Debye temperature  $\theta_D = 216$  K, as well as the Einstein modes  $\omega_{E1} = 51.4$  K and  $\omega_{E2} = 106.6$  K with frequency widths  $\Delta\omega$  of 1.5 and 3.5 K, respectively. The slightly lower Einstein branches derived from this fit compared to the pronounced  $g(\omega)$  features of our DFT calculation might be suspected to be due to the slightly smaller DFT unit cell parameters. However, this is not the case because the lower Einstein branches remain practically unchanged for small variations of the unit cell parameters.

From Fig. 11 one would assume that the Debye-like  $\omega^2$  behavior of the phonon DOS ends with the onset of the first Einstein mode at  $\sim 1.5$  THz. However, from Fig. 13 and especially from the inset it is seen that the phonon DOS starts to deviate from a Debye-like  $\omega^2$  behavior already at a much

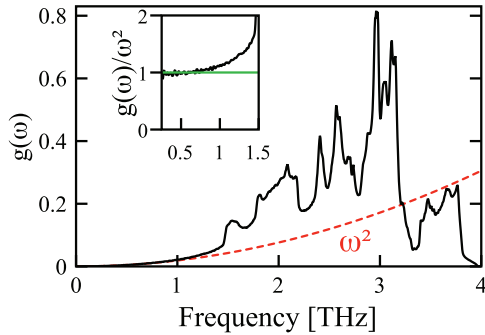


FIG. 13. (Color online) Phonon DOS [ $g(\omega)$ ] up to 4 THz (solid black line) compared to a Debye-like  $\omega^2$  behavior (gray/red dashed line). The inset shows  $g(\omega)/\omega^2$  versus frequency highlighting the deviations of  $g(\omega)$  from a Debye-like  $\omega^2$  behavior.

lower frequency of  $\sim 0.7$  THz. These deviations are attributed to a slight phonon softening that is also visible in the phonon dispersion along  $\Gamma$ -Z (Fig. 11). Such a specific feature, in combination with the large spectral weight at 1.5–2.2 THz, is expected to account for the disagreement between the Debye temperatures derived from specific heat and resistivity data.

By comparing the phonons from Figs. 11 and 13 to the Fermi surfaces shown in Figs. 8 and 9 one can identify unusual and important phonon modes that might play a crucial role for superconductivity. Electronic states with  $k_F$  on the closed hole Fermi surface around  $\Gamma$  can be paired by phonons  $\vec{q}$  (via  $\vec{k}_F + \vec{q} = -\vec{k}_F$ ) with frequencies of the lowest acoustic mode smaller than 1.2 THz, i.e., the range where the phonon DOS does not show a distinct peak, but deviations from Debye-like  $\omega^2$  behavior are already obvious. Electronic states with  $k_F$  on the remaining open tubes and pillar-like Fermi surfaces can be connected by phonons  $\vec{q}$  with frequencies of the lowest acoustic mode  $\sim 1.5$  THz (first Einstein mode) and  $\sim 2$  THz, both corresponding to pronounced peaks in the phonon DOS.

The moderate height of these peaks, however, might be the reason for the low superconducting transition temperature. Such a correlation has recently been shown for ternary  $APt_3P$  superconductors ( $A = \text{Ca}, \text{Sr}, \text{La}$ ) where the height of the low energy phonon DOS peak was in-line with the respective value of  $T_c$  (Ref. 34).

Concerning a possible unconventional behavior of LaPtSi, the above-described pairing results predominately in spin-singlets since the spin directions rotate concomitantly along the Fermi surface sheets with the electronic states at  $\vec{k}_F$  and  $-\vec{k}_F$  having opposite spins, as can be seen from Fig. 9. In this figure examples for spin-singlet pairing and simultaneous spin-singlet and spin-triplet pairing are also indicated. Spin-singlets (total spin of the Cooper pair  $S = 0$ ) are possible everywhere on the Fermi surface. Spin-triplets ( $S \neq 0$ ), although in principle allowed to coexist with spin-singlets due to the ASOC for noncentrosymmetric systems, are of much lesser importance for LaPtSi as they may only occur at Fermi surface intersections. This is completely in-line with the experimental observations.

#### IV. SUMMARY

Bulk properties like the temperature-dependent electrical resistivity, specific heat, or magnetization evidence superconductivity in LaPtSi below  $T_c = 3.35$  K. A thorough analysis of the experimental data reveals a fully gapped  $s$ -wave superconducting state. Examining  $l_{tr}/\xi \approx 0.92$ , we classify LaPtSi as a weakly coupled superconductor in the dirty limit. The value of  $\kappa_{GL} \approx 8.7$  refers to a type-II superconductor. DFT calculations derived both the electronic structure and phonon properties of LaPtSi. The absence of inversion symmetry in the crystal structure is responsible for a lifting of the two-fold degeneracy of the electronic bands, except in the  $\Gamma$ -Z direction. Superconductivity originates predominantly from Pt and La electronic states since Pt- $d$  and La- $d$  states dominate the electronic DOS at the Fermi energy. Specific  $\vec{q}$  vectors, associated with a softening of phonons in various directions in the reciprocal space (e.g.,  $\Gamma$ -Z',  $\Gamma$ -Z) are supposed to mediate superconductivity via  $\vec{k}_F + \vec{q} = -\vec{k}_F$ . Although there is a rather large spin-orbit splitting in LaPtSi, the topology of the Fermi surface enforces predominantly spin-singlet pairing. This seems to explain why unconventional superconductivity has not been observed experimentally for LaPtSi.

#### ACKNOWLEDGMENTS

This work was supported by the Austrian Science Fund FWF under Grant No. P22295. Calculations were done on the Vienna Scientific Cluster (VSC).

<sup>1</sup>E. Bauer, G. Hilscher, H. Michor, C. Paul, E. W. Scheidt, A. Gribanov, Y. Seropegin, H. Noël, M. Sigrist, and P. Rogl, *Phys. Rev. Lett.* **92**, 027003 (2004).

<sup>2</sup>H. Q. Yuan, D. F. Agterberg, N. Hayashi, P. Badica, D. Vandervelde, K. Togano, M. Sigrist, and M. B. Salamon, *Phys. Rev. Lett.* **97**, 017006 (2006).

<sup>3</sup>K. Klepp and E. Parthé, *Acta Cryst. B* **38**, 1105 (1982).

<sup>4</sup>J. Evers, G. Oehlinger, A. Weiss, and C. Probst, *Solid State Commun.* **50**, 61 (1984).

<sup>5</sup>S. Ramakrishnan, K. Ghosh, A. D. Chinchure, V. R. Marathe, and G. Chandra, *Phys. Rev. B* **52**, 6784 (1995).

<sup>6</sup>W. H. Lee and R. N. Shelton, *Phys. Rev. B* **35**, 5369 (1987).

<sup>7</sup>I. Zeiringer, A. Grytsiv, P. Brož, and P. Rogl, *J. Solid State Chem.* **196**, 125 (2012).

<sup>8</sup>G. Kresse and J. Furthmüller, *Phys. Rev. B* **54**, 11169 (1996).

<sup>9</sup>G. Kresse and D. Joubert, *Phys. Rev. B* **59**, 1758 (1999).

<sup>10</sup>P. E. Blöchl, *Phys. Rev. B* **50**, 17953 (1994).

<sup>11</sup>D. M. Ceperley and B. J. Alder, *Phys. Rev. Lett.* **45**, 566 (1980).

<sup>12</sup>H. Monkhorst and J. Pack, *Phys. Rev. B* **13**, 5188 (1976).

<sup>13</sup>D. Alfè, *Comp. Phys. Commun.* **180**, 2622 (2009).

<sup>14</sup>H. Bärnighausen, *Commun. Math.* **9**, 139 (1980).

- <sup>15</sup>H. Bärnighausen and U. Müller, Symmetriebeziehungen zwischen den Raumgruppen als Hilfsmittel zur straffen Darstellung von Strukturzusammenhängen in der Kristallchemie, University of Karlsruhe and University GH Kassel (1996).
- <sup>16</sup>J. Y. Chen, H. H. Sung, K. J. Syu, and W. H. Lee, *Physica C* **470**, 772 (2010).
- <sup>17</sup>A. H. Wilson, *Proc. R. Soc. Lond. A* **167**, 580 (1938).
- <sup>18</sup>N. F. Mott and H. Jones, *Theory of the Properties of Metals and Alloys* (Dover, New York, 1958), Chap. VII.
- <sup>19</sup>K. Togano, P. Badica, Y. Nakamori, S. Orimo, H. Takeya, and K. Hirata, *Phys. Rev. Lett.* **93**, 247004 (2004).
- <sup>20</sup>T. Klimczuk, Q. Xu, E. Morosan, J. D. Thompson, H. W. Zandbergen, and R. J. Cava, *Phys. Rev. B* **74**, 220502 (2006).
- <sup>21</sup>E. Bauer, R. T. Khan, H. Michor, E. Royanian, A. Grytsiv, N. Melnychenko-Koblyuk, P. Rogl, D. Reith, R. Podloucky, E.-W. Scheidt, W. Wolf, and M. Marsman, *Phys. Rev. B* **80**, 064504 (2009).
- <sup>22</sup>A. P. Pikul and D. Gnida, *Solid State Commun.* **151**, 778 (2011).
- <sup>23</sup>B. Mühlischlegel, *Z. Phys.* **155**, 313 (1959).
- <sup>24</sup>N. R. Werthamer, E. Hefland, and P. C. Hohenberg, *Phys. Rev.* **147**, 295 (1966).
- <sup>25</sup>K. Hummer, A. Grüneis, and G. Kresse, *Phys. Rev. B* **75**, 195211 (2007).
- <sup>26</sup>M. Weinert, E. Wimmer, and A. J. Freeman, *Phys. Rev. B* **26**, 4571 (1982).
- <sup>27</sup>M. Weinert, G. Schneider, R. Podloucky, and J. Redinger, *J. Phys.: Condens. Matter* **21**, 084201 (2009).
- <sup>28</sup>D. Reith, C. Blaas-Schenner, and R. Podloucky, *Phys. Rev. B* **86**, 104105 (2012).
- <sup>29</sup>J. Callaway, *Energy Band Theory* (Academic, New York, 1964), Chap. 1.
- <sup>30</sup>L. P. Gor'kov and E. I. Rashba, *Phys. Rev. Lett.* **87**, 037004 (2001).
- <sup>31</sup>W. L. McMillan, *Phys. Rev.* **167**, 331 (1968).
- <sup>32</sup>A. Junod, D. Bichsel, and J. Müller, *Helv. Phys. Acta* **52**, 580 (1979).
- <sup>33</sup>A. Junod, T. Jarlborg, and J. Müller, *Phys. Rev. B* **27**, 1568 (1983).
- <sup>34</sup>C.-J. Kang, K.-H. Ahn, K.-W. Lee, and B. I. Min, *J. Phys. Soc. Japan* **82**, 053703 (2013).